CANCER

Lighting up metastasis process before formation of secondary tumor by phosphorescence imaging

Kai Chang[1]†, Leyi Xiao[2]†, Yuanyuan Fan[1], Juqing Gu[1], Yunsheng Wang[3], Jie Yang[3], Mingzhou Chen[4], Yufeng Zhang[2]*, Qianqian Li[1]*, Zhen Li[1,3]*

Metastasis is the leading cause of cancer-related deaths; until now, the detection of tumor metastasis is mainly located at the period that secondary tumors have been formed, which usually results in poor prognosis. Thus, fast and precise positioning of organs, where tumor metastases are likely to occur at its earliest stages, is essential for improving patient outcomes. Here, we demonstrated a phosphorescence imaging method by organic nanoparticles to detect early tumor metastasis progress with microenvironmental changes, putting the detection period ahead to the formation of secondary tumors. In the orthotopic and simulated hematological tumor metastasis models, the microenvironmental changes could be recognized by phosphorescence imaging at day 3, after tumor implantation in liver or intravenous injection of cancer cells. It was far ahead those of other reported imaging methods with at least 7 days later, providing a sensitive and convenient method to monitor tumor metastases at the early stage.

INTRODUCTION

Cancer causes most deaths around the world, leading to estimated 10 million deaths worldwide in 2020 (*1*), and statistics suggest that the overwhelming majority of cancer-associated deaths (about 90%) are caused by metastatic disease, rather than primary tumors (*2*). Basically, the progression of metastases includes invasion, intravasation, circulation, and extravasation, eventually resulting in colocalization from a primary tumor (*3*–*6*). However, recent discoveries revealed that tumor metastases induce the change of microenvironment in distant organs, including vascular leakiness, the alteration of fibroblasts, and the recruitment of bone marrow–derived cells, which attracted circulating tumor cells (CTCs) and was conducive to the survival and growth before they reach these sites (*7*).

In general, diverse metastasis from different organs, such as liver, breast, kidney, colon, pancreas, and prostate can spread to lungs for the specialized microenvironment (*2*, *8*, *9*). Therefore, the diagnoses of premetastatic microenvironmental changes in lungs are the urgent demands to lay the foundation for prognosis and treatment, improving the opportunities of recovery (*6*). Unfortunately, although a great deal of research has been investigated to combat cancer metastasis, it is still a big challenge to achieve the diagnosis of metastatic process before the formation of secondary tumor as the early stage.

Until now, various in vivo imaging detection methods as noninvasive techniques have been developed to diagnose early metastases by recognition of the region of tumor lesions (*10*), such as fluorescence imaging (FLI) (*11*–*13*), photoacoustic imaging (*14*), magnetic resonance imaging (MRI) (*15*), positron emission tomography (PET) (*16*), and computed tomography (CT) (*17*). However, when the sizes of tumors are less than 1 cm, the commonly used PET and CT imaging techniques are clinically unreliable (*18*), while the relatively low sensitivity of MRI limited the detection process. For optical imaging techniques of FLI with rapid and sensitive response, the existence of autofluorescence as background signals largely decreased signal-to-noise ratios. Bioluminescence imaging (*19*) or chemiluminescence imaging (*20*, *21*) is usually influenced by reaction velocities and is heavily dependent on biodistribution of a particular substrate or enzyme. In addition, for practical reasons, neither routine use of biopsies nor assessment of all potential sites of metastasis is feasible (*18*), because metastases have already occurred before detection of primary tumor in most cases. Thus, the exploration of more effective imaging approaches with general applicability and high signal-to-noise ratios is urgently needed to meet the rapid developing requirements of early metastasis diagnoses.

Recently, organic room temperature phosphorescence (RTP) materials have emerged as the new generation of afterglow imaging agents, demonstrating good biocompatibility and high signal-to-noise ratios for avoiding autofluorescence in the in vivo imaging (*22*–*24*). Moreover, ultraviolet (UV) excitation process can be separated by the preirradiation process for persistent RTP materials (*25*), or replaced by phone flashlight excitation in red RTP emission systems (*26*), to shield the possible biological damage. Accordingly, the primary tumors, including liver, lung, and subcutaneous tumor, can be monitored by high signal-to-background ratio (SBR) and time-resolved phosphorescence imaging (*25*, *27*).

Considering these advantages mentioned above, here, we prepared phosphorescence nanoparticles (NPs) by phenothiazine derivatives, which exhibited ultrahigh brightness with a quantum yield of 22.9%. Moreover, phosphorescence lifetime of NPs can achieve up to 49 ms in aqueous solution, much longer than those of common RTP NPs (table S1), resulting in the naked eyes–observed afterglow in phosphate-buffered saline (PBS) solution

[1]Hubei Key Lab on Organic and Polymeric Opto-Electronic Materials, TaiKang Center for Life and Medical Sciences, Sauvage Centre for Molecular Sciences, Department of Chemistry, Wuhan University, Wuhan, China. [2]State Key Laboratory Breeding Base of Basic Science of Stomatology (Hubei-MOST) and Key Laboratory of Oral Biomedicine, Ministry of Education, School and Hospital of Stomatology, Wuhan University, Wuhan, China. [3]Institute of Molecular Aggregation Science, Tianjin University, Tianjin, China. [4]State Key Laboratory of Virology and Modern Virology Research Centre, Collage of Life Science, Wuhan University, Wuhan, China. *Corresponding author. Email: zyf@whu.edu.cn (Y.Z.); liqianqian@whu.edu.cn (Q.L.); lizhen@whu.edu.cn (Z.L.)
†These authors contributed equally to this work.

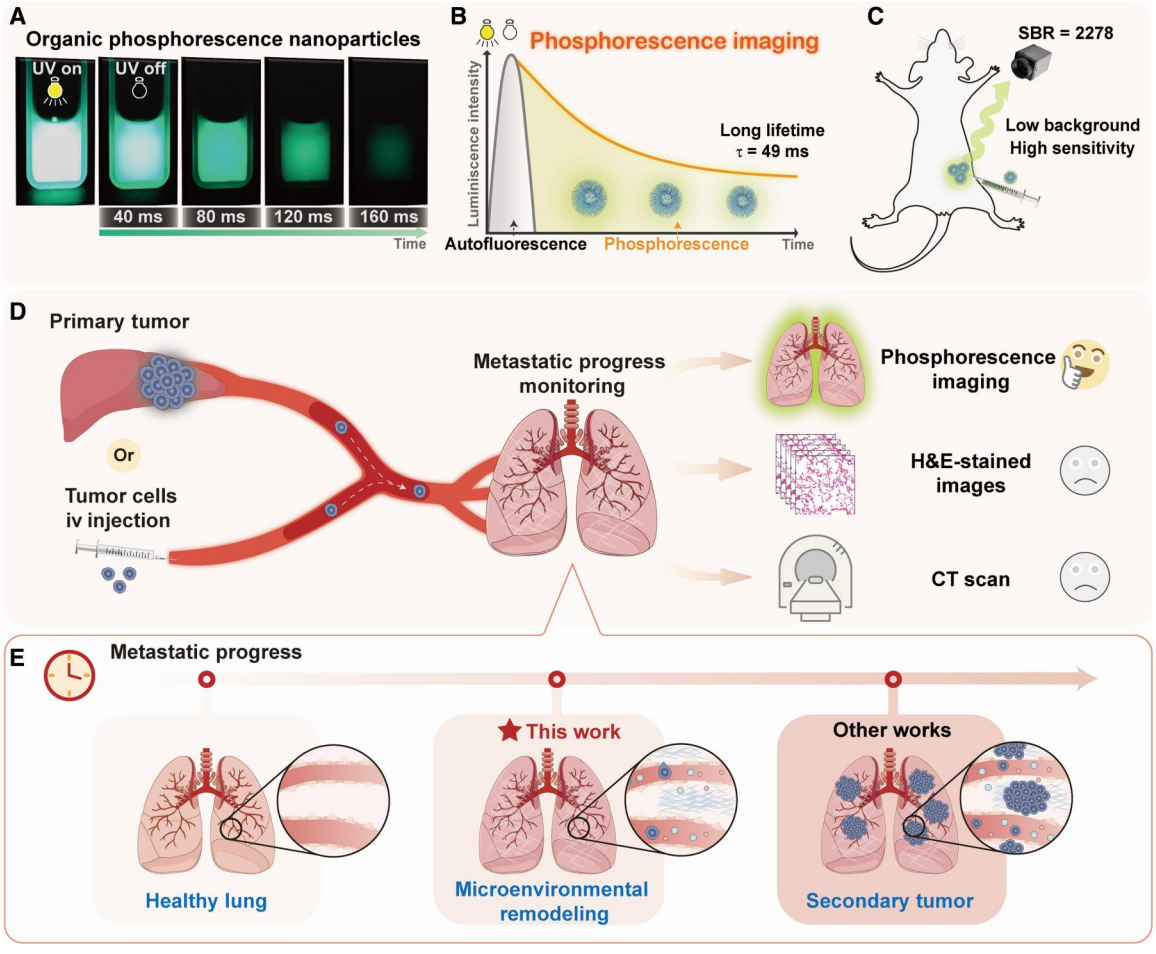

Fig. 1. Detection of tumor metastasis processes using pure organic phosphorescence imaging. (**A**) Photograph of pure organic phosphorescence NPs with ultrabright and persistent afterglow. (**B**) The schematic diagram of phosphorescence imaging, which can shield the autofluorescence for long lifetime. (**C**) The high SBR of phosphorescence NPs in in vivo imaging of living mice. (**D**) Metastatic progress from liver to lung or simulated by intravenous (iv) injection of tumor cells and detection of metastatic progress in lung by organic phosphorescence imaging, H&E-stained images, and CT scan. (**E**) Detailed tumor metastatic progress in lung with the passage of time, and the microenvironmental remodeling of metastatic progress can be recognized by phosphorescence imaging, far ahead of other works at secondary tumor stage.

(Fig. 1A). Once these NPs were applied into bioimaging, the high SBR of 2278 ± 242 in subcutaneous imaging has been achieved by effective avoidance of autofluorescence (Fig. 1, B and C), which is the highest one among the reported organic phosphorescence NPs so far. The early metastatic stage before the formation of secondary tumor can be lighted up and recognized by phosphorescence imaging (Fig. 1, D and E). It is defined as premetastatic changes of the microenvironment, which was confirmed by elevated expressions of transforming growth factor–β (TGF-β), tumor necrosis factor–α (TNF-α), and vascular endothelial growth factor (VEGF) by immunohistochemistry (IHC) (*5*, *28*, *29*), together with no obvious micrometastatic tumor in micro-CT and hematoxylin and eosin (H&E)–stained images, as well as slightly increased expression of the B cell lymphoma 2 (BCL-2) (*30*). Thus, the premetastatic microenvironmental changes were detected by afterglow imaging, much sensitive than those of the current imaging technologies, demonstrating the superiority of organic persistent RTP materials in the diagnoses of early process of metastasis (fig. S1 and table S1).

RESULTS

Preparation of phosphorescence NPs and in vitro imaging

The RTP NPs with modest hydrodynamic diameter (Fig. 2A and fig. S2) were prepared from phenothiazine derivatives and an amphiphilic triblock copolymer of PEG-b-PPG-b-PEG (F127) by a top-down method (fig. S3) (*31*), which exhibited naked eyes–observed green afterglow with a lasting time of 0.16 s in aqueous solution (Fig. 1A). It is an uncommon phenomenon for RTP NPs because phosphorescence of most of organic materials is easily quenched by oxygen and water in the common sense (*32*, *33*). In the host-guest system of phenothiazine derivatives, the strong intermolecular interactions between phenothiazine (guest) and corresponding dioxide (host) derivatives at the crystalline states can result in the formation of triplet exciplex with matched energy levels, contributing to persistent and bright RTP emission even under pure oxygen atmosphere (*25*). Moreover, fabrication of NPs with the top-down method as the preferred approach can retain the compact aggregated structure at crystalline state (fig. S4), resulting in strong resistance to oxygen even if the oxygen saturation is up to 80% (fig. S5). The

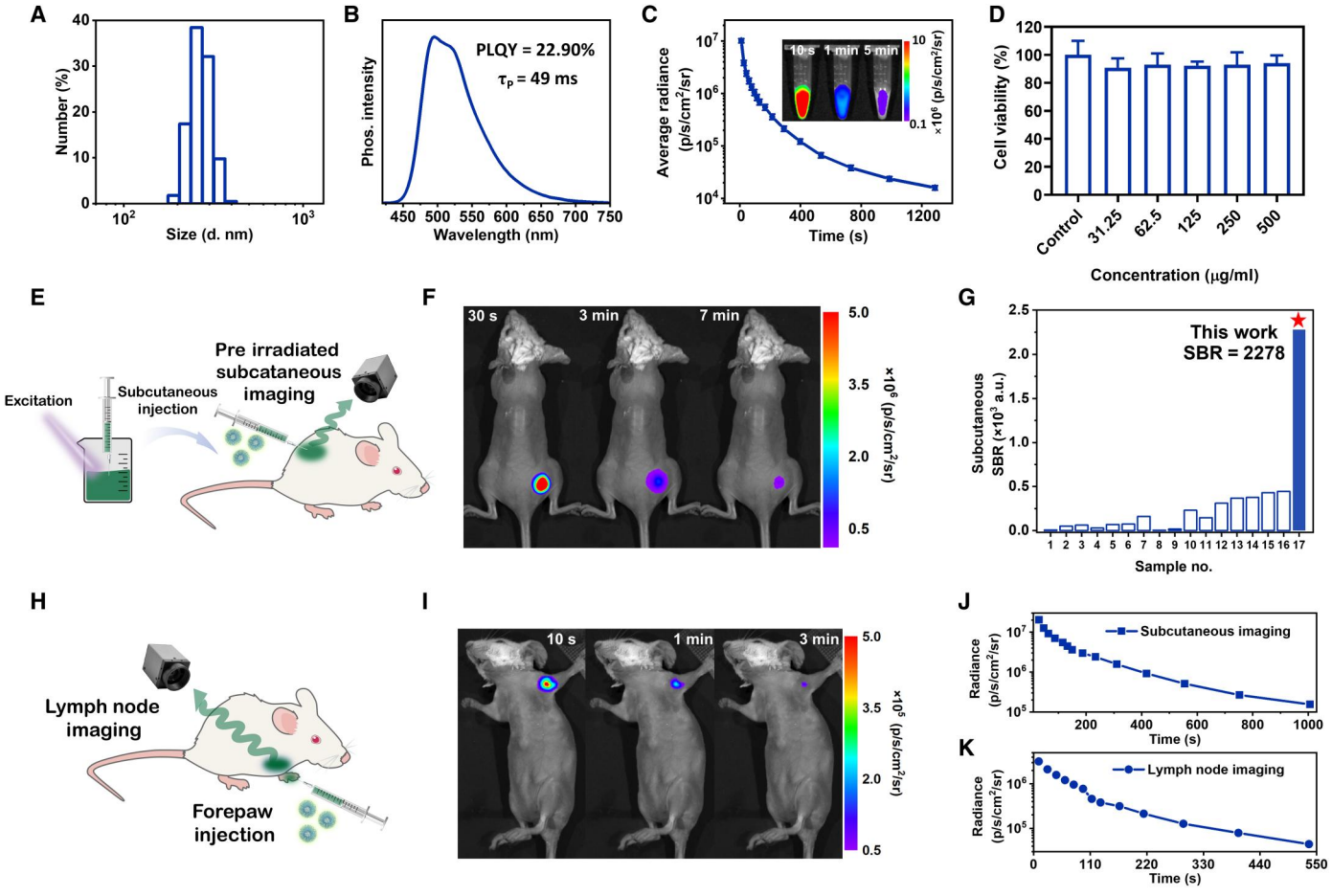

Fig. 2. Characterization, preirradiated subcutaneous imaging, and lymph nodes imaging of phosphorescence NPs. (**A**) Sizes and distribution of phosphorescence NPs by dynamic light scattering. (**B**) Phosphorescence spectrum, PLQY, and phosphorescence lifetime of NPs. (**C**) Time-dependent phosphorescence decay of NPs recorded after turning off the light irradiation, acquired using an IVIS instrument in bioluminescent mode. Inset: Phosphorescence images of NPs (4 mg ml^{-1}) with lasting times of 10 s, 1 min, and 5 min. (**D**) The viability of H22 cancer cells with the incorporation of NPs in different concentrations (n = 3; means ± SD). (**E**) Schematic diagram of preirradiated subcutaneous in vivo imaging of living mice. (**F**) Phosphorescence bioimaging of mice by subcutaneous injection of preirradiated NPs at lasting times of 30 s, 3 min, and 7 min using an IVIS instrument in bioluminescent mode (n = 3). (**G**) SBR of subcutaneous imaging by pure organic RTP materials reported in literatures and our work. Detailed sample names can be found in table S2. (**H**) Schematic diagram of lymph node imaging by forepaw injection of RTP NPs. (**I**) Phosphorescence bioimaging of mice after removal of light irradiation at t = 10 s, t = 1 min, and t = 3 min using an IVIS instrument in bioluminescent mode (n = 3). (**J** and **K**) Time-dependent phosphorescence decay of preirradiated subcutaneous imaging (J) and lymph nodes imaging (K) (n = 3). a.u., arbitrary units.

phosphorescence emission of NPs is mainly located at 495 nm (Fig. 2B), with the ultralong lifetime of 49 ms in aqueous solution (fig. S6), and the photoluminescence quantum yield (PLQY) achieved up to 22.9%. The persistent afterglow with high brightness results in the apparent phosphorescence images with an average radiance of 1.02 ± 0.1 × 10^7 p s^{-1} cm^{-2} sr^{-1} ex vivo. Moreover, the phosphorescence signal could last for more than 1200 s after removing excitation (Fig. 2C). NPs showed a good linear relationship between concentration and phosphorescence intensity (fig. S7), even when the concentration is extremely low (<1 μg ml^{-1}), beneficial to the sensitive emission response during the incipient accumulating process of NPs. The phosphorescence intensity of NPs enhanced with increased viscosity and rigidity by the addition of hyaluronic acid and gelatin, accompanying the slightly increased RTP lifetimes, which may facilitate the recognition of subtle changes in tissue stiffness (fig. S8). There is no substantial degradation of NPs over 8 cycles of repeated excitation, indicating good repeatability (fig. S9). Accordingly, no notable changes in phosphorescence intensity of NPs could be observed after eight cycles of activation or 80 min of UV irradiation (fig. S10A), showing strong resistance to photobleaching. Furthermore, the phosphorescence intensity of NPs was almost kept unchanged during incubation in PBS at 4°C for 28 days (fig. S10B), demonstrating good stability for long-term monitoring and storage (*34*).

Biocompatibility

The cytotoxicity of NPs was evaluated by the cell counting kit-8 (CCK-8) assay against H22, 4T1, and NIH/3T3 cells, demonstrating more than 90% cell viabilities even at the concentration as high as 500 μg ml^{-1} (Fig. 2D and fig. S11) (*35*). For mice treated with NPs, H&E-stained images of the main organs, including the hearts, livers, spleens, lungs, and kidneys, demonstrated no histological lesions (fig. S12). Moreover, the body weights of mice were not affected after the injection of NPs, indicating no obvious in vivo side

toxicities (fig. S13) (*36*). All these experimental results demonstrate that NPs have high biosafety, which is particularly promising for further bioimaging.

Subcutaneous and lymph node phosphorescence imaging

Subsequently, the in vivo bioimaging experiments were conducted, and the emission signal was collected using an IVIS spectrum instrument in bioluminescence mode with open filter (*37*). Owing to the excellent RTP performance of NPs, the preirradiated subcutaneous imaging can be realized to avoid the possible UV damage (Fig. 2E). The phosphorescence signal from NPs could be observed underneath the mouse skin at 30 s (Fig. 2F), and the in vivo phosphorescence imaging could last for more than 1000 s after the ceasing of light excitation (Fig. 2J). The SBR of subcutaneous phosphorescence imaging could reach to 2278 ± 242 (fig. S14A). To the best of our knowledge, it was the highest one for organic RTP imaging and about sixfolds of the highest value reported in the literatures (Fig. 2G and table S2) (*31*). Furthermore, lymph node imaging was carried out by forepaw injection of NPs into hair-removed BALB/c mice (Fig 2H) (*38*). The sentinel lymph node could be shown clearly (Fig. 2I) with a high SBR of 123 ± 17 (fig. S14B), and the phosphorescence signal could last for more than 500 s (Fig. 2K). Thus, ultrabright and persistent RTP NPs were proved as the excellent developing agent of optical imaging with high SBR and deep penetration.

Phosphorescence imaging and metabolism in lung metastases model

With the aim to preliminarily estimate the tumor-targeting ability of RTP NPs, the 4T1 lung metastases mouse model was established by intravenously injection of 4T1 cancer cells into BALB/c mice (Fig. 3A) (*39*). After 14 days, RTP NPs were intravenously injected; subsequently, phosphorescence imaging of major organs, including heart, liver, spleen, lung, and kidney, were carried out after 1.5, 3, 5, 7, 12, and 24 hours postinjection (Fig. 3B). Among them, only lungs exhibited a bright phosphorescence emission, indicating the high selectivity of RTP NPs toward metastatic lungs (fig. S15). The optimized interval time of 3 hours was proved by the maximum phosphorescence radiance with the highest SBR of 224 ± 53 (Fig. 3C), and the afterglow can last for 180 s. The superiority of phosphorescence imaging with high contrast and time resolution can be further confirmed by the corresponding FLI with low SBR (1 to 3; lung–to–normal liver) under the same conditions (Fig. 3D). Meanwhile, no obvious change can be found in H&E-stained images of major organs after injection of NPs (fig. S16), indicating good biocompatibility.

Afterward, metabolic experiments of NPs in major organs of mice bearing 4T1 lung metastases were carried out (*40*). At 1 hour postinjection, NPs mainly distributed in the reticuloendothelial system, which was proved by the higher concentrations of NPs in liver, spleen, and lung with 143 ± 15, 78 ± 17, and 120 ± 18 μg g^{-1}, respectively (fig. S17). Note that the concentration of NPs in livers was higher than that of lungs, but the phosphorescence intensity was much lower. Accordingly, NPs was incubated with different tissue homogenization and blood for 3 hours (fig. S18). Taking the phosphorescence emission of NPs in PBS solution as the reference (100%), the corresponding intensity can achieve 82 ± 6.3% in lung and 91 ± 8.3% in tumor; the high brightness is beneficial to phosphorescence imaging and subsequent detection in the lungs. For other organs, the intensity decreased to 60 ± 8.1% in liver, 66 ± 5.8% in spleen, 44 ± 6.5% in heart, 74 ± 3.1% in kidney, and 48 ± 3.1% in blood for the possible quenching effect by iron ion (*25*). At 72 hours postinjection, NPs were mostly metabolized with low concentrations in heart (17 ± 1.8 μg g^{-1}), liver (14 ± 0.7 μg g^{-1}), spleen (20 ± 4.9 μg g^{-1}), lung (30 ± 1.1 μg g^{-1}), and kidney (11 ± 1.3 μg g^{-1}). At 72 hours postinjection, NPs were mostly metabolized with low concentrations in heart (17 ± 1.8 μg g^{-1}), liver (14 ± 0.7 μg g^{-1}), spleen (20 ± 4.9 μg g^{-1}), lung (30 ± 1.1 μg g^{-1}), and kidney (11 ± 1.3 μg g^{-1}).

Recognition of premetastatic microenvironmental changes in lungs

As discussed above, phosphorescence NPs exhibited strong specificity toward metastatic lungs; combined with the advantages of negligible background interference by persistent afterglow, it was promising to be applied into early detection of metastasis in lung. Accordingly, the detection of metastatic progression by phosphorescence imaging was further conducted by tumor metastasis through blood flow, which is the major route of the spread of cancel cells (*41*, *42*). In this experiment, 4T1 cancer cells were intravenously injected into BALB/c mice at day 0 to establish a simulation of hematological metastasis model. Subsequently, phosphorescence imaging, micro-CT, and histopathological examinations, including H&E and IHC, were conducted every 3 to 4 days for the evaluation of metastatic progression in the lungs under the same experiment conditions. The maximum phosphorescence radiance ($3.5 \pm 0.8 \times 10^5$ p s^{-1} cm^{-2} sr^{-1}) at day 3 exhibited the statistically significant change ($P = 0.0070$), which was 3.1-folds of that in the control group (healthy BALB/c mice) (fig. S19). At this point (day 3), micro-CT and H&E-stained images did not show obvious changes, indicating the early metastatic stage, before the formation of secondary tumor was captured by phosphorescence imaging sensitively. In the following day 7 to day 14, phosphorescence imaging also showed good sensitivity for the maximum phosphorescence radiance increasing from $3.8 \pm 0.1 \times 10^5$ to $5.2 \pm 0.1 \times 10^5$ p s^{-1} cm^{-2} sr^{-1} and the calculated lung volume rising gradually from 435 ± 31 to 517 ± 15 mm^3.

With the aim to determine the definite biological processes as detected by phosphorescence imaging during tumor metastasis, the incidental variations of microenvironments have been investigated (*43*, *44*). In general, these variations are conducive to the survival and outgrowth of tumor cells before their arrival at these sites (*3*). Primary tumor-secreted soluble molecules play critical roles in preparation of distant sites for de novo formation of premetastatic niches (PMNs), thereby promoting metastasis processes. Tumor-derived secreted factors, such as TNF-α and TGF-β, along with VEGF in the lung can help the development of PMNs (*45*). The inhibition of apoptosis can result in abnormal overexpression of pro-survival Bcl-2 family members or abnormal reduction of proapoptotic Bcl-2 family proteins, which are frequently detected in diverse malignancies (*46*). Accordingly, the IHC technique was further used to investigate the expression of TGF-β, TNF-α, VEGF, and BCL-2 (*30*, *47*–*49*), accompanying tumor metastases progress. Average optical density (AOD) was used for the semiquantitative analysis of the expression of Bcl-2, TGF-β, TNF-α, and VEGF. From day 0 to day 14, the AOD rose from 0.08 ± 0.005 to 0.25 ± 0.01 for Bcl-2, from 0.17 ± 0.005 to 0.29 ± 0.01 for TGF-β, from 0.1 ± 0.02 to 0.44 ± 0.01 for TNF-α, and from 0.15 ± 0.02 to 0.31

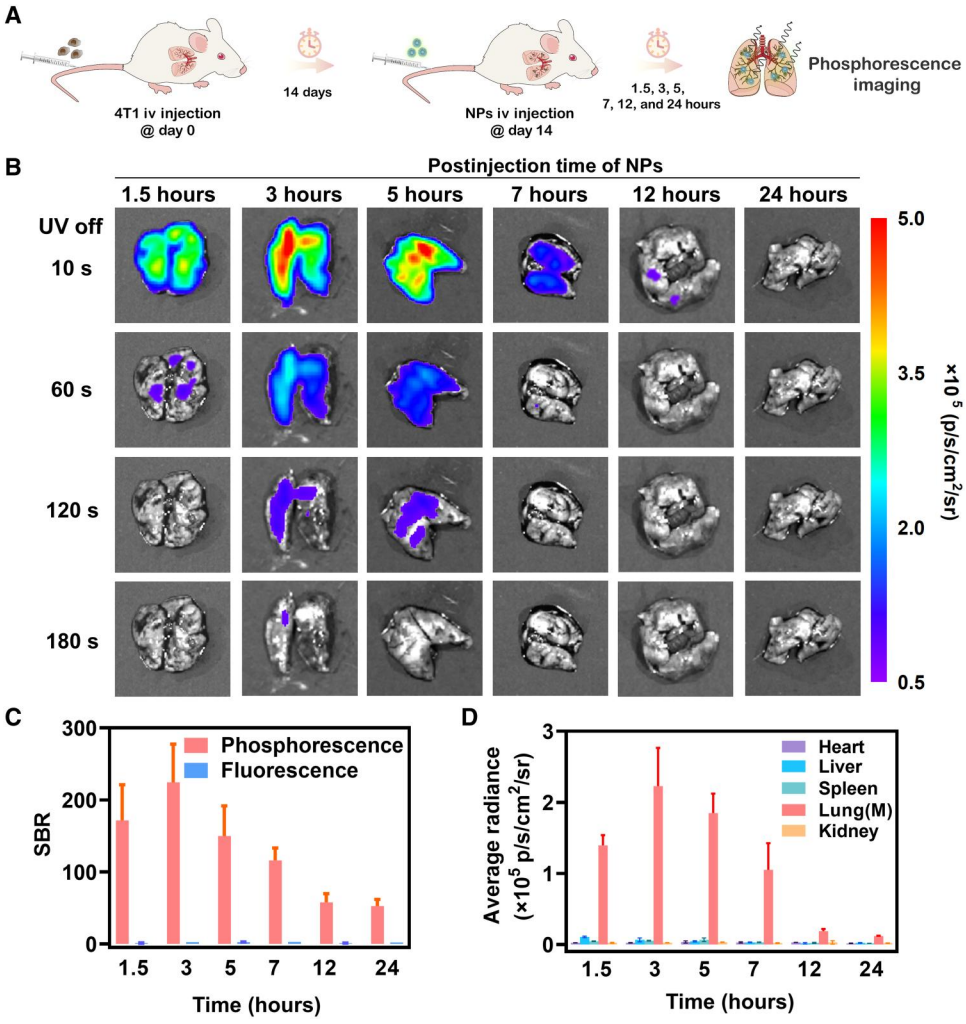

Fig. 3. Phosphorescence imaging in lung metastases model by intravenous injection of 4T1 cancer cells after 14 days. (**A**) Schematic diagram of establishment of lung metastatic mouse model and the following phosphorescence imaging. (**B**) Time-resolved phosphorescence imaging of isolated lungs from mice bearing 4T1 metastatic tumors at 1.5, 3, 5, 7, 12, and 24 hours postintravenous injection of NPs, after removal of light irradiation at t = 10 s, t = 60 s, t = 120 s, and t = 180 s using an IVIS instrument in bioluminescent mode (n = 3; means ± SD). (**C**) SBR of isolated lungs from mice bearing 4T1 metastatic tumors at 1.5, 3, 5, 7, 12, and 24 hours postintravenous injection of NPs after removal of light irradiation at t = 10 s (n = 3; means ± SD). (**D**) Average radiance of isolated organs (hearts, livers, spleens, lungs, and kidneys) from mice bearing 4T1 metastatic tumors at 1.5, 3, 5, 7, 12, and 24 hours postintravenous injection of NPs after removal of light irradiation at t = 10 s (n = 3; means ± SD).

± 0.01 for VEGF (figs. S21 and S22). The largely increased expression of BCL-2, TGF-β, TNF-α, and VEGF indicated that the definite metastatic progression from blood flow with obvious microenvironmental changes, as detected by phosphorescence imaging, is the metastatic niches of lungs (*18*). It is far ahead of other reported imaging methods, providing an efficient approach to the early diagnosis of tumor metastasis.

The possible tumor metastasis process from other organs to lung can also be sensitively monitored by phosphorescence imaging. Accordingly, H22 liver tumors were implanted into the liver of BALB/c mice at day 0 to establish tumor metastasis model from liver to lung. The degree of metastases in the lungs was detected by phosphorescence imaging, micro-CT, and histopathological examinations synchronously every 3 to 4 days until day 27 (Fig. 4A). For phosphorescence imaging at 3 hours after intravenous injection of NPs (4 mg ml^{-1}, 200 μl), the maximum phosphorescence radiances of lungs gradually rose from day 0 to day 27, meaning that NPs progressively enriched in lungs during this period (*48*). On day 3, statistical analysis showed that the maximum phosphorescence radiance ($1.5 \pm 0.1 \times 10^5$ p s^{-1} cm^{-2} sr^{-1}) exhibited statistically significant change (P = 0.0321), with healthy mice without tumor implantation as the control group. At this time, no obvious metastatic tumor signals were monitored in H&E-stained images. Moreover, the lung volume calculated from micro-CT and H&E-stained images of lung did not show an apparent difference (Fig. 4, B to D). On day 7 and day 10, the maximum phosphorescence radiances continuously rose to $1.7 \pm 0.2 \times 10^5$ and $1.8 \pm 0.2 \times 10^5$ p s^{-1} cm^{-2} sr^{-1}, respectively, showing statistically significant difference (P = 0.0110 and 0.0066). The maximum phosphorescence radiance increased to $3.0 \pm 0.3 \times 10^5$ p s^{-1} cm^{-2} sr^{-1} on day 27, suggesting that significant changes have taken place in the pulmonary microenvironment. As the control experiments, the maximum

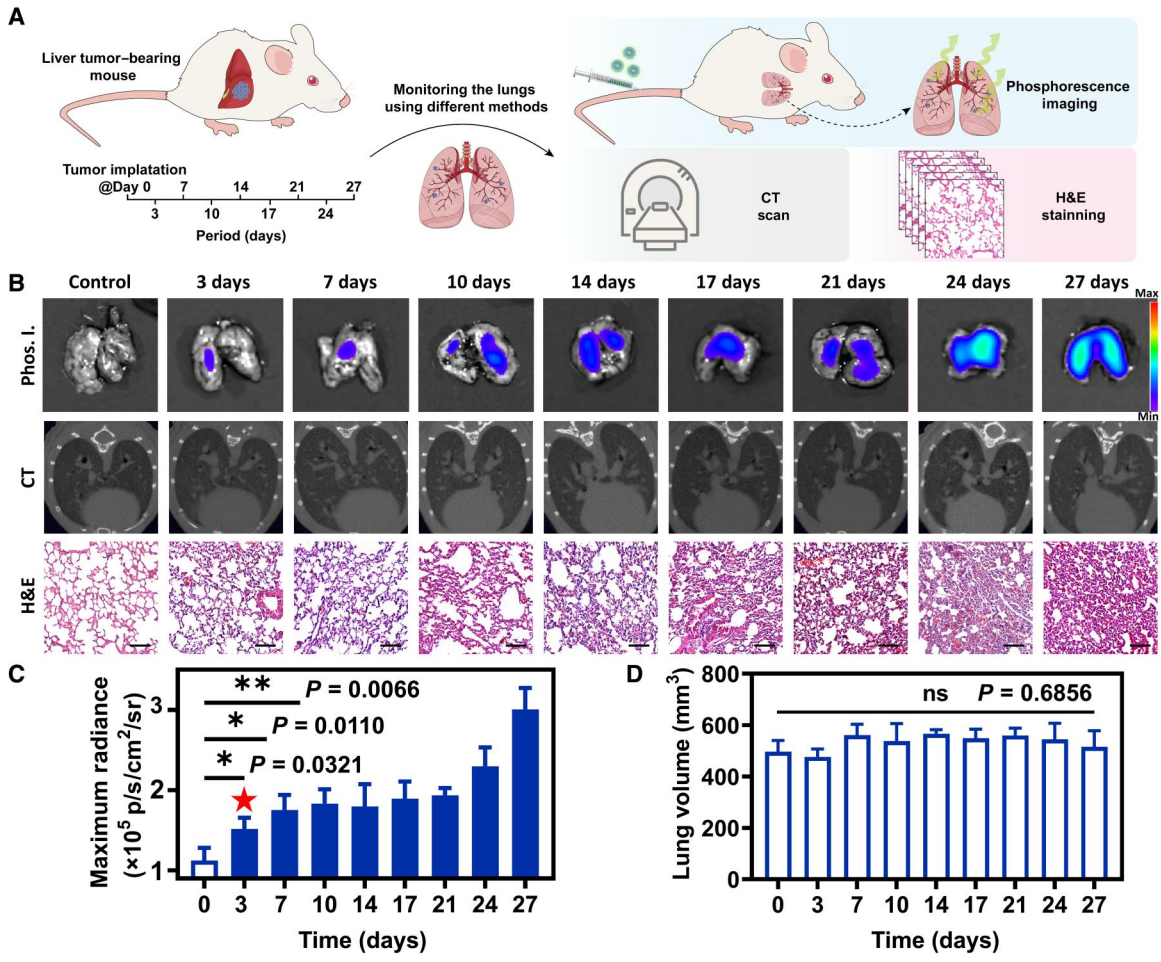

Fig. 4. Detection of tumor metastatic processes by phosphorescence imaging. (**A**) Schematic diagram of in situ implantation of liver tumor and detection of microenvironmental changes in lungs by phosphorescence imaging, CT scan, and pathological sections. (**B**) Phosphorescence imaging (Phos. I.), CT images, and H&E-stained images of metastatic lungs from day 0 to day 27. Scale bars, 100 μm. (**C**) Maximum radiance of phosphorescence imaging of lungs from day 0 to day 27 (n = 3). (**D**) Lung volume of lungs from day 0 today 27 calculated by Analyze 14.0 software (n = 3; means ± SD). ns, not significant, *P < 0.05, and **P < 0.01.

phosphorescence radiance of healthy BALB/c mice was virtually unchanged from day 0 to day 27 (fig. S23).

The expression of TGF-β, TNF-α, and VEGF were significantly enhanced from day 0 to day 27 (Fig. 5A), with AOD increasing from 0.16 ± 0.01 to 0.34 ± 0.04 for TGF-β, 0.11 ± 0.01 to 0.36 ± 0.03 for TNF-α, and 0.15 ± 0.01 to 0.33 ± 0.02 for VEGF (Fig. 5, B to I, and fig. S23). On day 3, P values of AOD were 0.0002, <0.0001, and 0.0005 for TGF-β, TNF-α, and VEGF, respectively, indicating that the microenvironment of the lungs has been significantly modified, and PMNs have been formed (*18*). Meanwhile, the expression of BCL-2 increased slightly with an AOD of 0.13 ± 0.02, compared to that of 0.11 ± 0.01 on day 0 (P = 0.908), which means the arrival of a small quantity of CTCs from liver cancer after PMNs. Thus, the definite metastasis processes detected by phosphorescence imaging were also the metastatic niches of lungs (*18*).

These experiments indicated that, regardless of the approaches of metastatic processes, the metastatic niches of lung can be recognized rapidly and sensitively by phosphorescence imaging. The early stage of tumor metastasis before the formation of secondary tumors is monitored by a universal approach, thus alerting the opportunity for the quick cure.

DISCUSSION

By using phosphorescence NPs of organic molecules with the ultralong lifetime and ultrahigh brightness, the microenvironmental changes in tumor metastasis process, before the formation of secondary tumors, can be detected by phosphorescence imaging of lung with high SBR. It is far ahead of other reported imaging methods, and the universality of sensitive phosphorescence detection can be confirmed by the metastasis model from orthotopic liver tumor to lung, as well as lung metastasis model through blood flow. The detection of tumor metastasis at an early stage can be helpful to discontinue the formation of secondary tumors and possible deterioration largely, affording more chance to the cure for cancer. Moreover, in comparison with the commonly used immunohistochemical staining in the laboratory, the macroscopic resolution by phosphorescence imaging can facilitate the detection process by

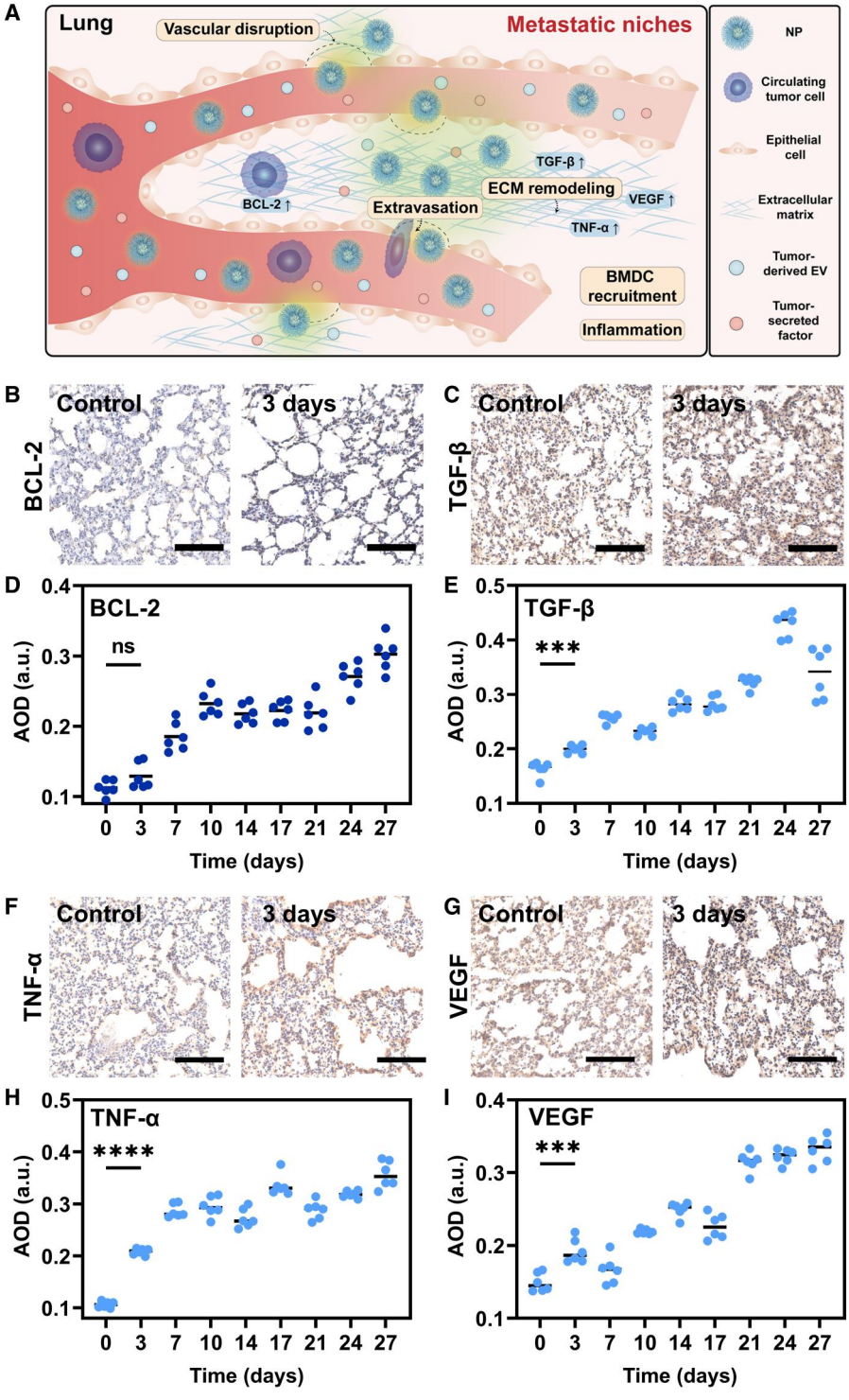

Fig. 5. IHC analysis. (**A**) Schematic diagram of metastatic niches. (**B**, **C**, **F**, and **G**) IHC staining of Bcl-2 (B), TGF-β (C), TNF-α (F), and VEGF (G) of metastatic lungs on day 0 and day 3 ($n = 3$). Scale bars, 100 μm. (**D**, **E**, **H**, and **I**) AOD of the corresponding IHC-stained images calculated by ImageJ software: Bcl-2 (D), TGF-β (E), TNF-α (H), and VEGF (I) ($n = 6$). ns, not significant, ***$P < 0.001$, and ****$P < 0.0001$.

eliminating the tedious slicing process, promoting further clinical applications with low cost and rapid response.

MATERIALS AND METHODS

Chemicals and bioreagents

All reagents used in the experiments were purchased from commercial sources without further purification. The amphiphilic copolymer PEG-b-PPG-b-PEG (F127) was purchased from Sigma-Aldrich Ltd. and used as received. Tetrahydrofuran (THF) was dried using K-Na alloy through distillation under an atmosphere of dry argon.

Material characterization

Photoluminescence and excitation spectra were recorded with a Hitachi F-4600 fluorescence spectrophotometer or FLS980 spectrometer. Photoluminescence lifetimes and quantum yield were measured with a FLS980 spectrometer under ambient conditions. Dynamic light scattering and zeta potential were measured on a Malvern Nano-ZS90 Zetasizer. Transmission electron microscope images were captured on a JEM-2100 Plus transmission electron microscope with an accelerating voltage of 120 kV. In vitro and in vivo phosphorescence imaging were conducted on IVIS Spectrum imaging system (PerkinElmer Inc.; the cooling temperature of charge-coupled device lens is −90°C). A dissolved oxygen analyzer (JPSJ-605F, Oustor Inc.) was equipped to evaluate the oxygen saturation in aqueous solution.

Preparation of NPs

F127 (10 mg) and M-PhCl crystals (1 mg) were dissolved in THF (1 ml), and then THF was evaporated with a gentle nitrogen flow. Then, deionized water (3 ml) was added, and the mixture was sonicated using a microtip-equipped probe ultrasonic instrument (Scientz-IID) for 20 min (duty cycle of 80%) to afford a NP solution (0.33 mg ml^{-1}). The obtained NP solution was stored at 4°C in the dark.

In vitro phosphorescence imaging

The phosphorescence intensities of NPs were recorded using IVIS Spectrum system at t = 10 s after irradiating using a 365-nm handheld UV lamp with the power density of 127 mW cm^{-2} for 3 s. The IVIS system was set in bioluminescence mode with open filter (exposure time: 17 s).

Photostability study

NPs was irradiated using a white light flashlight with the power density of 283 mW cm^{-2} for 3 s with varying exposure times of 0, 20, 40, 60, and 80 min. The phosphorescence intensities were recorded using IVIS system in bioluminescence mode with open filter (exposure time: 17 s).

Cell culture

NIH/3T3 cells were acquired from the American Type Culture Collection and cultured in DMEM (Dulbecco's modified Eagle's medium) (GIBCO) supplemented with 10% fetal bovine serum (FBS) and 1% penicillin-streptomycin (Hyclone) at 37°C under humid conditions with 5% CO_2. 4T1 breast cancer cells and H22 mice hepatoma cells were acquired from the American Type Culture Collection and cultured in RPMI 1640 (GIBCO) supplemented with 10% FBS and 1% penicillin-streptomycin (Hyclone) at 37°C in a humidified environment containing 5% CO_2.

Cytotoxicity study

In vitro cytotoxicity of NPs against NIH/3T3 cells and H22 mice hepatoma cells were evaluated by the CCK-8 assay (HY-K0301, MedChemExpress). NIH/3T3 cells and H22 mice hepatoma cells were seeded in a 96-well cell culture plate with 1×10^4 cells per well, while NIH/3T3 cells needed incubating overnight for attachment. Then, cells were exposed to the NPs at the various concentrations of 6.25, 12.5, 25, 50, 100 μg ml^{-1}, with another group of 1× PBS as the control. After 24 hours of incubation, the wells of NIH/3T3 cells were washed twice with 1× PBS, while the H22 group left out this step. The culture medium diluted 1:10 with CCK-8 assay was added 110 μl into each well. Then, the media were transferred to a new 96-well cell culture plate, and the absorbance was measured using a microplate reader scanning at 450 nm for BALB/cJGpt mice (strain no. N000020).

Animals and tumor models

Six-week-old female BALB/cJGpt mice (strain no. N000020) were purchased from the Gempharmatech Co. Ltd. (Chengdu, China). Mice were maintained in specific pathogen–free grade animal room at ~25°C, with humidity ranging from 40 to 60%, on a standard 12-h light–12-h dark cycle (lights on at 6:00 or 7:00) and fed ad libitum.

To set up the orthotopic liver tumor-bearing mouse model, the BALB/c mice were injected subcutaneously in the right flank region with 100 μl of cell suspension containing 5×10^6 H22 hepatoma cells. When the tumor volume reached around 500 mm^3, the mice were euthanized and the H22 tumor tissues were harvested. The tumor tissue was cut into small pieces of around 1 mm^3. The orthotopic hepatoma model was constructed by surgical implantation of the small tumor tissue about 1 mm^3 into the liver of healthy BALB/c mice.

To establish the pulmonary metastatic carcinoma–bearing mouse model, 1×10^6 4T1 cancer cells in 100 μl of cell culture medium were injected into the healthy BALB/c mice via tail vein. After about 14 days, the pulmonary metastatic tumors were formed with nodules scattering in the lung.

Statement of ethical approval

All animal studies were performed according to the guidelines, and the overall project protocols were approved by the Welfare and Ethics Committee of Laboratory Animal, College of Life Sciences, Wuhan University (approval no. WDSKY0202101).

In vivo side toxicity study

Healthy BALB/c mice were used to evaluate the in vivo toxicity of NPs, which were randomly assigned into two groups (n = 3 per group). Then, 200 μl of NPs (4 mg ml^{-1} based on NPs) was injected into each healthy mouse in one group via the tail vein, and for another group, 200 μl of PBS was injected as control. The weights of mice in two groups were monitored within 20 days. At day 20 postinjection, all the mice in two groups were euthanized, and the normal tissues including liver, spleen, and kidneys of each mouse were excised, which were subsequently fixed in 4% neutral paraformaldehyde buffer, processed routinely into paraffin, sliced at

thickness of 5 μm, and stained with H&E. The H&E-stained slices were imaged by optical microscopy and assessed by three independent pathologists.

Subcutaneous phosphorescence imaging with preirradiated NPs

The healthy BALB/c mice were anesthetized with 1% sodium pentobarbital in PBS and placed into the box of the IVIS instrument. Then, NPs were preirradiated by 365-nm hand-held UV lamp with a power density of 127 mW cm^{-2} for 3 s. After that, 100 μl of the activated NPs (1 mg ml^{-1} based on NPs) was subcutaneously injected into the mice, followed by imaging with IVIS instrument at different time points. The phosphorescence images were acquired in bioluminescence mode with open filter (exposure time: 17 s). During the imaging process, the mice were warmed with a heating pad under continued isoflurane anesthesia.

Phosphorescence imaging of sentinel lymph node

Fifty microliters of NPs (1 mg ml^{-1} based on NPs) was injected into the forepaws of live BALB/c mice. At 30 min postinjection, after the mice were anesthetized with 1% sodium pentobarbital, the axillae of mice were irradiated using a 365-nm hand-held UV lamp with a power density of 127 mW cm^{-2} for 3 s (UV dose: 3.81 J m^{-2}) and then imaged with IVIS instrument in bioluminescence mode with open filter (exposure time: 17 s) at 10 s after stoppage of light excitation.

Phosphorescence imaging of pulmonary metastatic tumors

Two hundred mircoliters of NPs (4 mg ml^{-1} based on NPs) were injected into pulmonary metastatic carcinoma–bearing mice via the tail vein. At 1.5, 3, 5, 7, 12, and 24 hours postinjection, the tumor-bearing mice were euthanized, and the main organs including heart, lung, spleen, kidneys, and liver with tumors were excised. These organs were irradiated using a 365-nm hand-held UV lamp (127 mW cm^{-2}) for 3 s and then imaged with an IVIS instrument in bioluminescence mode with open filter (exposure time: 17 s) at 10 s after stoppage of light excitation. FLI was also conducted with the IVIS instrument in fluorescence mode. These tissues were subsequently fixed in 4% neutral paraformaldehyde buffer, processed routinely to sliced, and stained with H&E. The H&E-stained slices were imaged by optical microscopy and assessed by three independent pathologists.

Phosphorescence imaging of metastatic progression in lungs

For the metastases in lungs from orthotopic liver tumor, the tumor-bearing mice were randomly divided into nine groups (n = 3 per group) at the day of tumor implantation (day 0). After every 3 or 4 days until day 27, 200 μl of NPs (4 mg ml^{-1} based on NPs) was injected into one group of mice via the tail vein at each point of time. At 3 hours postinjection, the tumor-bearing mice were euthanized, and main organs including heart, lung, spleen, kidneys, and liver with tumors were excised. These organs were irradiated using a 365-nm hand-held UV lamp (127 mW cm^{-2}) for 3 s and then imaged with an IVIS instrument in bioluminescence mode with open filter (exposure time: 17 s) at 10 s after stoppage of light excitation. Furthermore, these tissues were subsequently fixed in 4% neutral paraformaldehyde buffer, processed routinely to sliced, and stained with H&E. The H&E-stained slices were imaged by optical microscopy and assessed by three independent pathologists. For the simulated hematological metastases in lungs, healthy BALB/c mice were randomly divided into five groups (n = 3 per group) at the day of 4T1 injection (day 0), followed by phosphorescence imaging in the same condition as mentioned above.

Immunohistochemical staining

The tissue was fixed in 4% neutral paraformaldehyde buffer over 2 days and subsequently embedded in paraffin. The tissues were sliced 5 μm after stored in 4°C for 1 hour. The tissue sections were baked at 65°C for 60 min before rehydration with graded alcohols and then deparaffinized in dimethylbenzene and rehydrated. Sections were repaired with an antigenic repair solution (MXB Biotechnologies) for half an hour at 37°C and washed with 1× PBS for three times. IHC staining was performed in a process on the sections using a polyclonal antibody against Bcl-2, TGF-β, TNF-α, and VEGF (ABclonal). 3,3′-Diaminobenzidine (DAB) IHC slides were scanned at ×20 on the Aperio VERSA 8 digital scanner (Leica Biosystems, Milton Keynes, UK).

Micro-CT scan of metastases in lungs

At each of these time points, micro-CT of metastases in lung was carried out for every mouse in groups (n = 3) by using Quantum GX2 microCT imaging system, with a field of view of 45 mm in the high-resolution scan mode. During this time, the tumor-bearing mice were anesthetized using 2% isoflurane in oxygen.

Biodistribution assay of NPs in vivo

Two hundred miroliters of NPs (4 mg ml^{-1} based on NPs) was injected into mice bearing lung metastasis via the tail vein. At 1, 3, 5, 7, 9, 24, and 72 hours after injection, the mice were euthanized, and various organs (heart, liver, spleen, lung with metastasis, and kidney) were excised and weighted. For each time point, three mice were tested. The organs were suspended in dichloromethane and intensely homogenized. After kept in the dark for 24 hours, the suspensions were filtered and the air-equilibrated filtrations were measured on the UV-visible spectrophotometer with absorption at 315 nm. The concentrations of NPs in the filtrations were calculated, according to the standard curves. Three mice of intravenous injection with PBS were used as the blank group. The values measured from the organs of the blank group served as the background and were deducted from the corresponding sample of the administrated mice.

Statistical analysis

The in vitro, in vivo, and ex vivo fluorescence and phosphorescence signals were quantified with region of interest analysis using Living Image 4.7.2 software (PerkinElmer Inc.). Micro-CT scan was conducted with Quantum GX software (PerkinElmer Inc.), and calculation of lung volumes was carried out using Analyze 14.0 software (AnalyzeDirect Inc.). All experiments were repeated independently more than three times. Results are expressed as the mean ± SD unless stated otherwise. Investigators were blinded to group allocation during experiments. Statistical comparisons were determined between two groups by t test. For all tests, P values less than 0.05 were considered statistically significant ($^{*}P < 0.05$, $^{**}P < 0.01$, $^{***}P < 0.001$, and $^{****}P < 0.0001$). All statistical calculations were performed using Origin 2022 learning edition (OriginLab Corporation) or GraphPad Prism 9.0 (GraphPad Software). All IHC images

were quantified by AOD using ImageJ (National Institutes of Health).

Supplementary Materials

This PDF file includes:

Figs. S1 to S23
Tables S1 and S2
References

View/request a protocol for this paper from *Bio-protocol*.

REFERENCES AND NOTES

1. R. L. Siegel, K. D. Miller, H. E. Fuchs, A. Jemal, Cancer statistics, 2021. *CA Cancer J. Clin.* **71**, 7–33 (2021).
2. S. Valastyan, R. A. Weinberg, Tumor metastasis: Molecular insights and evolving paradigms. *Cell* **147**, 275–292 (2011).
3. J. Massague, A. C. Obenauf, Metastatic colonization by circulating tumour cells. *Nature* **529**, 298–306 (2016).
4. W. Yu, C. Hu, H. Gao, Advances of nanomedicines in breast cancer metastasis treatment targeting different metastatic stages. *Adv. Drug Deliv. Rev.* **178**, 113909 (2021).
5. P. S. Steeg, Targeting metastasis. *Nat. Rev. Cancer* **16**, 201–218 (2016).
6. Y. Liu, X. Cao, Characteristics and significance of the pre-metastatic niche. *Cancer Cell* **30**, 668–681 (2016).
7. D. F. Quail, J. A. Joyce, Microenvironmental regulation of tumor progression and metastasis. *Nat. Med.* **19**, 1423–1437 (2013).
8. A. Schroeder, D. A. Heller, M. M. Winslow, J. E. Dahlman, G. W. Pratt, R. Langer, T. Jacks, D. G. Anderson, Treating metastatic cancer with nanotechnology. *Nat. Rev. Cancer* **12**, 39–50 (2011).
9. N. K. Altorki, G. J. Markowitz, D. Gao, J. L. Port, A. Saxena, B. Stiles, T. McGraw, V. Mittal, The lung microenvironment: An important regulator of tumour growth and metastasis. *Nat. Rev. Cancer* **19**, 9–31 (2019).
10. S. P. Rowe, M. G. Pomper, Molecular imaging in oncology: Current impact and future directions. *CA Cancer J. Clin.* **72**, 333–352 (2022).
11. H. Xiong, H. Zuo, Y. Yan, G. Occhialini, K. Zhou, Y. Wan, D. J. Siegwart, High-contrast fluorescence detection of metastatic breast cancer including bone and liver micrometastases via size-controlled pH-activatable water-soluble probes. *Adv. Mater.* **29**, 1700131 (2017).
12. P. Wang, Y. Fan, L. Lu, L. Liu, L. Fan, M. Zhao, Y. Xie, C. Xu, F. Zhang, NIR-II nanoprobes in-vivo assembly to improve image-guided surgery for metastatic ovarian cancer. *Nat. Commun.* **9**, 2898 (2018).
13. Y. Li, S. Zeng, J. Hao, Non-invasive optical guided tumor metastasis/vessel imaging by using lanthanide nanoprobe with enhanced down-shifting emission beyond 1500 nm. *ACS Nano* **13**, 248–259 (2019).
14. H. Cao, L. Zou, B. He, L. Zeng, Y. Huang, H. Yu, P. Zhang, Q. Yin, Z. Zhang, Y. Li, Albumin biomimetic nanocorona improves tumor targeting and penetration for synergistic therapy of metastatic breast cancer. *Adv. Funct. Mater.* **27**, 1605679 (2017).
15. P. Mi, D. Kokuryo, H. Cabral, H. Wu, Y. Terada, T. Saga, I. Aoki, N. Nishiyama, K. Kataoka, A pH-activatable nanoparticle with signal-amplification capabilities for non-invasive imaging of tumour malignancy. *Nat. Nanotechnol.* **11**, 724–730 (2016).
16. L. Hao, N. Rohani, R. T. Zhao, E. M. Pulver, H. Mak, O. J. Kelada, H. Ko, H. E. Fleming, F. B. Gertler, S. N. Bhatia, Microenvironment-triggered multimodal precision diagnostics. *Nat. Mater.* **20**, 1440–1448 (2021).
17. P. M. Peiris, R. Toy, E. Doolittle, J. Pansky, A. Abramowski, M. Tam, P. Vicente, E. Tran, E. Hayden, A. Camann, A. Mayer, B. O. Erokwu, Z. Berman, D. Wilson, H. Baskaran, C. A. Flask, R. A. Keri, E. Karathanasis, Imaging metastasis using an integrin-targeting chain-shaped nanoparticle. *ACS Nano* **6**, 8783–8795 (2012).
18. H. Peinado, H. Zhang, I. R. Matei, B. Costa-Silva, A. Hoshino, G. Rodrigues, B. Psaila, R. N. Kaplan, J. F. Bromberg, Y. Kang, M. J. Bissell, T. R. Cox, A. J. Giaccia, J. T. Erler, S. Hiratsuka, C. M. Ghajar, D. Lyden, Pre-metastatic niches: Organ-specific homes for metastases. *Nat. Rev. Cancer* **17**, 302–317 (2017).
19. M. Keyaerts, V. Caveliers, T. Lahoutte, Bioluminescence imaging: Looking beyond the light. *Trends Mol. Med.* **18**, 164–172 (2012).
20. W. Chen, Y. Zhang, Q. Li, Y. Jiang, H. Zhou, Y. Liu, Q. Miao, M. Gao, Near-infrared afterglow luminescence of chlorin nanoparticles for ultrasensitive in vivo imaging. *J. Am. Chem. Soc.* **144**, 6719–6726 (2022).
21. J. Huang, K. Pu, Activatable molecular probes for second near-infrared fluorescence, chemiluminescence, and photoacoustic imaging. *Angew. Chem. Int. Edit.* **59**, 11717–11731 (2020).
22. W. Zhao, Z. He, B. Z. Tang, Room-temperature phosphorescence from organic aggregates. *Nat. Rev. Mater.* **5**, 869–885 (2020).
23. M. Fang, J. Yang, Z. Li, Light emission of organic luminogens: Generation, mechanism and application. *Prog. Mater. Sci.* **125**, 100914 (2022).
24. A. Huang, Q. Li, Z. Li, Molecular uniting set identified characteristic (MUSIC) of organic optoelectronic material. *Chin. J. Chem.* **40**, 2356–2370 (2022).
25. Y. Wang, H. Gao, J. Yang, M. Fang, D. Ding, B. Z. Tang, Z. Li, High performance of simple organic phosphorescence host–guest materials and their application in time-resolved bioimaging. *Adv. Mater.* **33**, 2007811 (2021).
26. Y. Fan, S. Liu, M. Wu, L. Xiao, Y. Fan, M. Han, K. Chang, Y. Zhang, X. Zhen, Q. Li, Z. Li, Mobile phone flashlight-excited red afterglow bioimaging. *Adv. Mater.* **34**, 2201280 (2022).
27. F. Xiao, H. Gao, Y. Lei, W. Dai, M. Liu, X. Zheng, Z. Cai, X. Huang, H. Wu, D. Ding, Guest-host doped strategy for constructing ultralong-lifetime near-infrared organic phosphorescence materials for bioimaging. *Nat. Commun.* **13**, 186 (2022).
28. L. Wan, K. Pantel, Y. Kang, Tumor metastasis: Moving new biological insights into the clinic. *Nat. Med.* **19**, 1450–1464 (2013).
29. A. W. Lambert, D. R. Pattabiraman, R. A. Weinberg, Emerging biological principles of metastasis. *Cell* **168**, 670–691 (2017).
30. A. R. Delbridge, S. Grabow, A. Strasser, D. L. Vaux, Thirty years of BCL-2: Translating cell death discoveries into novel cancer therapies. *Nat. Rev. Cancer* **16**, 99–109 (2016).
31. X. Zhen, Y. Tao, Z. An, P. Chen, C. Xu, R. Chen, W. Huang, K. Pu, Ultralong phosphorescence of water-soluble organic nanoparticles for in vivo afterglow imaging. *Adv. Mater.* **29**, 1606665 (2017).
32. Y. Wang, J. Yang, M. Fang, Y. Gong, J. Ren, L. Tu, B. Z. Tang, Z. Li, New phenothiazine derivatives that exhibit photoinduced room-temperature phosphorescence. *Adv. Funct. Mater.* **31**, 2101719 (2021).
33. Q. Li, Z. Li, Molecular packing: Another key point for the performance of organic and polymeric optoelectronic materials. *Acc. Chem. Res.* **53**, 962–973 (2020).
34. X. Wu, Y. Jiang, N. J. Rommelfanger, F. Yang, Q. Zhou, R. Yin, J. Liu, S. Cai, W. Ren, A. Shin, K. S. Ong, K. Pu, G. Hong, Tether-free photothermal deep-brain stimulation in freely behaving mice via wide-field illumination in the near-infrared-II window. *Nat. Biomed. Eng.* **6**, 754–770 (2022).
35. Q. Dang, Y. Jiang, J. Wang, J. Wang, Q. Zhang, M. Zhang, S. Luo, Y. Xie, K. Pu, Q. Li, Z. Li, Room-temperature phosphorescence resonance energy transfer for construction of near-infrared afterglow imaging agents. *Adv. Mater.* **32**, 2006752 (2020).
36. C. Zhang, Z. Zeng, D. Cui, S. He, Y. Jiang, J. Li, J. Huang, K. Pu, Semiconducting polymer nano-PROTACs for activatable photo-immunometabolic cancer therapy. *Nat. Commun.* **12**, 2934 (2021).
37. Z. Cong, M. Han, Y. Fan, Y. Fan, K. Chang, L. Xiao, Y. Zhang, X. Zhen, Q. Li, Z. Li, Ultralong blue room-temperature phosphorescence by cycloalkyl engineering. *Mater. Chem. Front.* **6**, 1606–1614 (2022).
38. J. Yang, X. Zhen, B. Wang, X. Gao, Z. Ren, J. Wang, Y. Xie, J. Li, Q. Peng, K. Pu, Z. Li, The influence of the molecular packing on the room temperature phosphorescence of purely organic luminogens. *Nat. Commun.* **9**, 840 (2018).
39. H. Gao, Z. Gao, D. Jiao, J. Zhang, X. Li, Q. Tang, Y. Shi, D. Ding, Boosting room temperature phosphorescence performance by alkyl modification for intravital orthotopic lung tumor imaging. *Small* **17**, 2005449 (2021).
40. N. Bertrand, P. Grenier, M. Mahmoudi, E. M. Lima, E. A. Appel, F. Dormont, J.-M. Lim, R. Karnik, R. Langer, O. C. Farokhzad, Mechanistic understanding of in vivo protein corona formation on polymeric nanoparticles and impact on pharmacokinetics. *Nat. Commun.* **8**, 777 (2017).
41. G. Francia, W. Cruz-Munoz, S. Man, P. Xu, R. S. Kerbel, Mouse models of advanced spontaneous metastasis for experimental therapeutics. *Nat. Rev. Cancer* **11**, 135–141 (2011).
42. C. Liang, L. Xu, G. Song, Z. Liu, Emerging nanomedicine approaches fighting tumor metastasis: Animal models, metastasis-targeted drug delivery, phototherapy, and immunotherapy. *Chem. Soc. Rev.* **45**, 6250–6269 (2016).
43. B. A. Aguado, G. G. Bushnell, S. S. Rao, J. S. Jeruss, L. D. Shea, Engineering the pre-metastatic niche. *Nat. Biomed. Eng.* **1**, 0077 (2017).
44. G. R. Doak, K. L. Schwertfeger, D. K. Wood, Distant relations: Macrophage functions in the metastatic niche. *Trends Cancer* **4**, 445–459 (2018).
45. S. Hiratsuka, A. Watanabe, Y. Sakurai, S. Akashi-Takamura, S. Ishibashi, K. Miyake, M. Shibuya, S. Akira, H. Aburatani, Y. Maru, The S100A8-serum amyloid A3-TLR4 paracrine cascade establishes a pre-metastatic phase. *Nat. Cell Biol.* **10**, 1349–1355 (2008).
46. D. Kaloni, S. T. Diepstraten, A. Strasser, G. L. Kelly, BCL-2 protein family: Attractive targets for cancer therapy. *Apoptosis* **28**, 20–38 (2023).

47. T. Jiang, L. Chen, Y. Huang, J. Wang, M. Xu, S. Zhou, X. Gu, Y. Chen, K. Liang, Y. Pei, Q. Song, S. Liu, F. Ma, H. Lu, X. Gao, J. Chen, Metformin and docosahexaenoic acid hybrid micelles for premetastatic niche modulation and tumor metastasis suppression. *Nano Lett.* **19**, 3548–3562 (2019).
48. S. Hiratsuka, S. Ishibashi, T. Tomita, A. Watanabe, S. Akashi-Takamura, M. Murakami, H. Kijima, K. Miyake, H. Aburatani, Y. Maru, Primary tumours modulate innate immune signalling to create pre-metastatic vascular hyperpermeability foci. *Nat. Commun.* **4**, 1853 (2013).
49. S. Hiratsuka, A. Watanabe, H. Aburatani, Y. Maru, Tumour-mediated upregulation of chemoattractants and recruitment of myeloid cells predetermines lung metastasis. *Nat. Cell Biol.* **8**, 1369–1375 (2006).
50. W. Zhang, S. Song, H. Wang, Q. Wang, D. Li, S. Zheng, Z. Xu, H. Zhang, J. Wang, J. Sun, In vivo irreversible albumin-binding near-infrared dye conjugate as a naked-eye and fluorescence dual-mode imaging agent for lymph node tumor metastasis diagnosis. *Biomaterials* **217**, 119279 (2019).
51. Y. Wu, J. Chen, L. Sun, F. Zeng, S. Wu, A nanoprobe for diagnosing and mapping lymphatic metastasis of tumor using 3D multispectral optoacoustic tomography owing to aggregation/deaggregation induced spectral change. *Adv. Funct. Mater.* **29**, 1807960 (2019).
52. X. Zhu, H. Xiong, Q. Zhou, Z. Zhao, Y. Zhang, Y. Li, S. Wang, S. Shi, A pH-activatable $MnCO_3$ nanoparticle for improved magnetic resonance imaging of tumor malignancy and metastasis. *ACS Appl. Mater. Interfaces* **13**, 18462–18471 (2021).
53. X. Huang, F. Zhang, S. Lee, M. Swierczewska, D. O. Kiesewetter, L. Lang, G. Zhang, L. Zhu, H. Gao, H. S. Choi, G. Niu, X. Chen, Long-term multimodal imaging of tumor draining sentinel lymph nodes using mesoporous silica-based nanoprobes. *Biomaterials* **33**, 4370–4378 (2012).
54. J. Yang, Y. Zhang, X. Wu, W. Dai, D. Chen, J. Shi, B. Tong, Q. Peng, H. Xie, Z. Cai, Y. Dong, X. Zhang, Rational design of pyrrole derivatives with aggregation-induced phosphorescence characteristics for time-resolved and two-photon luminescence imaging. *Nat. Commun.* **12**, 4883 (2021).
55. T. Zhang, H. Gao, A. Lv, Z. Wang, Y. Gong, D. Ding, H. Ma, Y. Zhang, W. Z. Yuan, Hydrogen bonding boosted the persistent room temperature phosphorescence of pure organic compounds for multiple applications. *J. Mater. Chem. C* **7**, 9095–9101 (2019).
56. J. Yang, H. Gao, Y. Wang, Y. Yu, Y. Gong, M. Fang, D. Ding, W. Hu, B. Z. Tang, Z. Li, The odd–even effect of alkyl chain in organic room temperature phosphorescence luminogens and the corresponding in vivo imaging. *Mater. Chem. Front.* **3**, 1391–1397 (2019).
57. Q. Liao, Q. Gao, J. Wang, Y. Gong, Q. Peng, Y. Tian, Y. Fan, H. Guo, D. Ding, Q. Li, Z. Li, 9,9-Dimethylxanthene derivatives with room-temperature phosphorescence: Substituent effects and emissive properties. *Angew. Chem. Int. Edit.* **59**, 9946–9951 (2020).
58. Z. He, H. Gao, S. Zhang, S. Zheng, Y. Wang, Z. Zhao, D. Ding, B. Yang, Y. Zhang, W. Z. Yuan, Achieving persistent, efficient, and robust room-temperature phosphorescence from pure organics for versatile applications. *Adv. Mater.* **31**, 1807222 (2019).

Acknowledgments

Funding: This work was supported by the National Natural Science Foundation of China (22122504, 22235006, and 51973162), Foundation of Hubei Scientific Committee (2022BAA015 and 2020CFA084) and Wuhan City (whkxjsj014), and the Fundamental Research Funds for the Central Universities (2042202kf0031). All animal studies were performed according to the guidelines, and the overall project protocols were approved by the Welfare and Ethics Committee of Laboratory Animal, College of Life Sciences, Wuhan University (approval no. WDSKY0202101). **Author contributions:** Conceptualization: Q.L. and Z.L. Methodology: K.C. and L.X. Investigation: K.C., L.X., Y.F., J.G., Y.W., and J.Y. Visualization: K.C. and L.X. Supervision: Y.Z., Q.L., and Z.L. Funding acquisition: Q.L. and Z.L. Project administration: M.C., Y.Z., Q.L., and Z.L. Writing—original draft: K.C., L.X., and Q.L. Writing—review and editing: Y.Z., Q.L., and Z.L. **Competing interests:** The authors declare that they have no competing interests. **Data and materials availability:** All data needed to evaluate the conclusions in the paper are present in the paper and/or the Supplementary Materials.

Submitted 6 November 2022
Accepted 14 April 2023
Published 17 May 2023
10.1126/sciadv.adf6757